



Seasonal and interannual variability of the wave climate at a wave energy hotspot off the southwestern coast of Australia



Michael V.W. Cuttler ^{a, b, d, *}, Jeff E. Hansen ^{c, d}, Ryan J. Lowe ^{a, b, c, d}

^a Oceans Graduate School and UWA Oceans Institute, The University of Western Australia, M470, 35 Stirling Highway, Crawley, WA, 6009, Australia

^b ARC Centre of Excellence for Coral Reef Studies, The University of Western Australia, M004, 35 Stirling Highway, Crawley, WA, 6009, Australia

^c School of Earth Sciences, The University of Western Australia, M004, 35 Stirling Highway, Crawley, WA, 6009, Australia

^d Wave Energy Research Centre, The University of Western Australia – Albany Centre, 35 Stirling Terrace, Albany, WA, 6330, Australia

ARTICLE INFO

Article history:

Received 17 January 2019

Received in revised form

30 June 2019

Accepted 9 August 2019

Available online 11 August 2019

Keywords:

Wave energy

Wave climate

SWAN

Southern ocean

Southwestern Australia

Southern Annular Mode

ABSTRACT

Despite Australia having one of the most abundant offshore wave energy resources globally, there remains a lack of understanding of how this offshore resource extends into the coastal zone where most wave energy converters would be deployed. We used the phase-averaged wave model SWAN to simulate 38 years (1980–2017) of wave conditions near Albany, Western Australia, which has been proposed as a future commercial wave energy development site. The nearshore (30 m depth) wave resource varied seasonally and interannually with the wave energy flux and mean wave direction negatively correlated to the phase of the Southern Annular Mode (SAM) and positively correlated to the latitudinal position of the subtropical high-pressure ridge. As a result, the observed positive trend in SAM over recent decades may cause a decrease in nearshore wave energy (including fewer storm events) and an anti-clockwise (more southerly) rotation in wave direction. These changes may facilitate wave energy development and extraction by reducing the number and magnitude of extreme events during which wave energy cannot be extracted and equipment can be damaged. The interannual fluctuations in the wave resource can be significant and should be considered during the site selection for wave energy projects.

© 2019 Elsevier Ltd. All rights reserved.

1. Introduction

Australia is widely recognized as having an abundant wave energy resource due to the proximity and exposure of Australia's south coast to Southern Ocean swell [1,2]. The vicinity of the Southern Ocean makes Australia, and specifically the southern coast of Australia, one of the largest potential wave energy resources globally (Fig. 1) [2–4]. In recognition of this significant resource, the Australian government has recently made significant investments into wave energy development [4]. However, previous resource assessments (both national and regional) have been constrained by relatively low spatial resolutions and/or coverage [4], and are therefore, unable to resolve the wave transformations that govern nearshore wave climates in sufficient detail to quantify the wave energy resource for specific development sites.

Characterization of wave energy resources can be done at a range of temporal and spatial scales to meet the variety of interests across a range of stakeholders (e.g. developers, consumers, etc.), including: (1) reconnaissance, (2) feasibility, and (3) design-scale; with each successive level requiring more detailed information [5]. The Centre for Australian Weather and Climate Research (CAWCR), a collaboration between the Commonwealth Scientific and Industrial Research Organisation (CSIRO) and the Australian Bureau of Meteorology (BOM), have produced a national-scale, 31-year hindcast dataset (1979–2010) designed to deliver the information needed for reconnaissance-level resource assessments as well as provide the boundary conditions for the higher-resolution numerical models needed to conduct feasibility and design-scale resource assessments [4]. The CAWCR hindcast is continually updated (now 1979–2018, typically delayed ~1–2 months) [6] and thus, provides an opportunity to conduct detailed resource assessments and long-term wave climate analyses for locations all around Australia.

The Albany region of Western Australian has been targeted as a site for future development of wave energy; however, there is a significant knowledge gap pertaining to the nearshore wave

* Corresponding author. Oceans Graduate School and UWA Oceans Institute (M470), The University of Western Australia, 35 Stirling Highway, Crawley, WA, 6009, Australia.

E-mail address: michael.cuttler@uwa.edu.au (M.V.W. Cuttler).

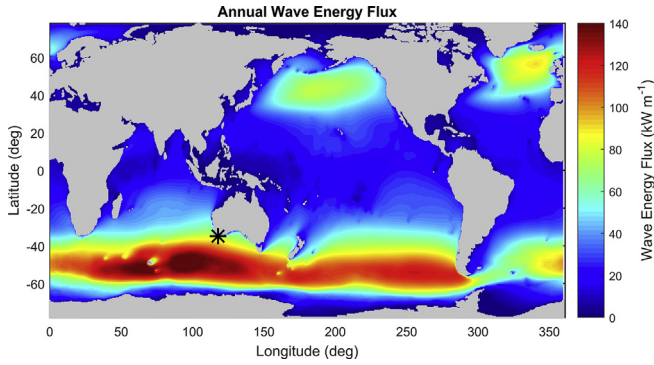


Fig. 1. Global mean annual wave energy flux (kW m^{-1}) calculated from the CAWCR reanalysis product from 1980 to 2017. The black asterisk denotes the study area near Albany, Western Australia.

climate and wave energy resource along the southern Australian margin. Previous wave resource assessments [4,7,8] and wave climate studies [9,10] have included this region, yet they have been conducted at large spatial scales (e.g. kilometres) and thus have lacked the high-resolution data needed to accurately predict the nearshore wave climate at specific locations along the southern Australian coastline. To provide the most useful information for device design and feasibility of large-scale wave energy production to prospective wave energy developers, these coarse offshore observations need to be transformed to the nearshore, where most devices will be deployed, to quantify the wave resource and its variability.

Here we present an analysis of the local wave climate incident to a site near Albany, Western Australia with specific emphasis on the implications for development of renewable wave energy. We used the CAWCR hindcast dataset to force a third-generation numerical wave model (Simulating WAVes Nearshore, SWAN) over a 38-year hindcast (1980–2017) to quantify the seasonal and interannual variability in the nearshore wave climate and wave energy resource. These results were compared to relevant climate indices (e.g. Southern Annular Mode, subtropical high-pressure ridge, Southern Oscillation Index) to understand their relationship to the long-term nearshore wave climate variability and how this could impact the potential wave energy resource.

2. Methods

2.1. Study area

The study site is located at Torbay in the Albany region of Western Australia (WA), ~415 km southeast of Perth (Fig. 2). Torbay is a south-western facing embayment that is directly exposed to incident wave energy from the Southern Ocean (SO). The wave climate along the WA coastline is dominated by three major atmospheric systems: the SO storm belt [10,11], the subtropical high-pressure systems: the SO storm belt [10,11], the subtropical high-pressure ridge [12,13], and a local sea breeze system [14].

The SO storm belt (or the ‘roaring forties’) is characterised by strong westerly winds and a long fetch that generates eastward traveling swells. The fluctuating position of the SO storm belt has been shown to influence the variability of the wave heights and wave directions along the southern Australian coastline [9,10]. The position of the SO storm belt is closely correlated to the latitudinal position of the subtropical high-pressure ridge (STRP; a band of high pressure in the mid-latitudes of the Southern Hemisphere), which can influence local rainfall [15] and regional wave climate [13]. The seasonal northward shift in the STRP in winter is typically associated with larger waves as the northward position allows

westerly fronts from the SO storm belt to impact the WA region [12,13]. At a more local, nearshore scale, the WA region is impacted by diurnal sea breeze cycles in the summer months that have been shown to influence to the seasonal morphodynamics of WA beaches [14,16].

2.2. Wave model

The wave climate at Torbay was assessed through a 38-year hindcast (1980–2017) using the numerical wave model SWAN. SWAN is a 3rd-generation, phase-averaged wave model that solves the wave action balance equation without restrictions on spectral evolution due to wind growth [17]:

$$\frac{\delta \tilde{N}}{\delta t} + \frac{\delta c_\lambda \tilde{N}}{\delta \lambda} + \frac{\delta c_\varphi \tilde{N}}{\delta \varphi} + \frac{\delta c_\sigma \tilde{N}}{\delta \sigma} + \frac{\delta c_\theta \tilde{N}}{\delta \theta} = \frac{S_{tot}}{\sigma} \quad (1)$$

where the first term on the left-hand side represents the rate of change of the action density (\tilde{N}) in time (t). The next two terms represent the propagation of action density in space (Cartesian or spherical coordinates), where c_λ and c_φ are the propagation velocity in λ - and φ -space. The last two terms represent the spectral evolution of wave frequency (σ) and wave direction (θ), respectively, due to bathymetric variability and currents, where c_σ and c_θ is the propagation velocity in σ - and θ -space [17,18]. The right-hand side of Equation (1) represents all physical processes that can generate, dissipate, or redistribute wave energy:

$$S_{tot} = S_{wind} + S_{nl3} + S_{nl4} + S_{fric} + S_{brk} + S_{wcap} \quad (2)$$

These processes include local wind growth of waves (S_{wind}), nonlinear triad (S_{nl3}) and quadruplet (S_{nl4}) wave-wave interactions, and wave dissipation due to friction (S_{fric}), depth-induced breaking (S_{brk}), and white capping (S_{wcap}).

Three nested domains of varying resolution (500×500 m, 165×165 m, $50 \text{ m} \times 50 \text{ m}$; Fig. 2b and c) were used to simulate the propagation of waves from deep water to the proposed development site in 30 m depth (approximately 1.2 km offshore). Model bathymetry was derived from all available sources including: 50 m resolution multibeam national grid of Australia [19], spot sounding surveys collected by the Australian Hydrographic Office (AHO; chart AUS00118), and 3 m resolution bathymetric LiDAR (Fugaro LADS). When combining bathymetric datasets, preference was given to the LiDAR data (for depths less than 30 m), followed by the AHO data (due to spatial coverage in depths between 30 m and 300 m), and finally, the Geoscience Australia multibeam data was used for all depths greater than 300 m. All bathymetric data were referenced to the Australian Height Datum (AHD, approximately mean sea level).

SWAN was forced at the boundaries by hourly two-dimensional spectra derived from the CAWCR global wind-wave hindcast [4]. The CAWCR reanalysis is a WaveWatch III [20] wave model forced by Climate Forecast System Reanalysis (CFSR) wind data (0.3-degree resolution), that has been optimized for the Australian and South Pacific regions [4,21]. There exist some known biases in the upper percentile CFSR winds in the Southern Hemisphere during the early part of the CAWCR record (i.e. pre-1993), which can cause over-prediction of wave heights (~0.3 m) in the Southern Ocean [21–23]. However, these biases have not been reported to skew previous resource assessments for other parts of Australia [4,24] or assessments of climate variability on global surface waves [25] that have used the CAWCR hindcast dataset.

The frequency and directional domains in SWAN were discretised into 43 logarithmically spaced frequency bands between 0.04 and 0.6 Hz, and 108 equally spaced directional bins (i.e. $\sim 3^\circ$).

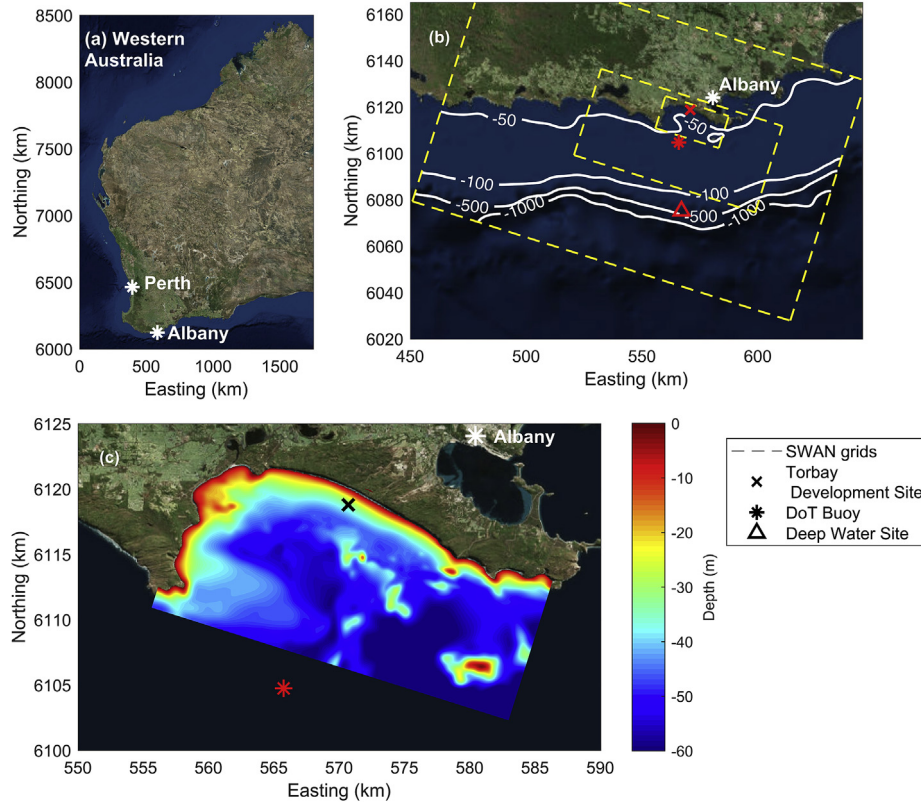


Fig. 2. (a) Western Australia (WA) with Perth and Albany indicated. (b) Overview of the study area and numerical model domains (yellow dashed lines), including the outer-most domain (500 × 500 m resolution), inner domain (165 × 165 m resolution), and nearshore grid (50 × 50 m resolution). (c) Nearshore bathymetry highlighting the complex features (e.g. submerged and exposed islands). In (b) and (c), the WA Department of Transport directional wave rider buoy is denoted by an asterisk (60 m depth) and development site and location of AWAC (30 m depth) denoted by 'x'. In (b), the location of the deep water site (~350 m depth) used for assessing offshore wave climate is denoted by the triangle. (For interpretation of the references to colour in this figure legend, the reader is referred to the Web version of this article.)

The directional resolution was set to account for the refraction of waves around the various headlands and shoals common across the study area (Fig. 2). Hourly winds at 10 m above the sea surface were also extracted from the gridded CAWCR outputs (~7 km resolution) and applied to the local SWAN domains. The relatively high temporal and spatial resolution of the wind forcing was needed to capture both the local generation of wind waves and the diurnal variability in local winds common around Western Australia [14]. Frictional dissipation (S_{fric}), was modelled using the default value for swell-dominated seas of 0.038 [26], and dissipation due to white-capping (S_{wcap}), was modelled following van der Westhuysen [27]. Non-linear triad (S_{nl3}) and quadruplet (S_{nl4}) wave-wave interactions were included using the default settings [28,29]. Non-stationary SWAN simulations were run with a 30-min time step for the entire time period using the hourly forcing conditions described above. Data was output every hour and included significant wave height (H_{sig}), mean period (T_m), mean wave direction (D_m), the horizontal components of the wave energy flux (E_x and E_y), and the two-dimensional spectra at locations corresponding to observational data. These parameters are calculated directly from wave spectra ($E(\sigma, \theta)$) output by SWAN as:

$$H_{sig} = 4 \sqrt{\iint E(\sigma, \theta) d\sigma d\theta} \quad (3)$$

$$T_m = 2\pi \frac{\iint E(\sigma, \theta) d\sigma d\theta}{\iint \sigma E(\sigma, \theta) d\sigma d\theta} \quad (4)$$

$$D_m = \frac{180}{\pi} \tan^{-1} \left(\frac{\int \sin(\theta) E(\sigma, \theta) d\sigma d\theta}{\int \cos(\theta) E(\sigma, \theta) d\sigma d\theta} \right) \quad (5)$$

$$E_{x,y} = \rho g \iint c_{x,y} E(\sigma, \theta) d\sigma d\theta \quad (6)$$

$$E_{mag} = \sqrt{E_x^2 + E_y^2} \quad (7)$$

2.3. Model output analysis

The model was validated against a Datawell Mark III directional waverider buoy in 60 m depth (July 2005 to present; maintained by Western Australia Department of Transport, DoT) and a Nortek AWAC deployed at 30 m depth (December 2017 to March 2018). Although we only utilize model data from January 1980 to December 2017 to avoid incomplete years, we simulated wave conditions through to March 2018 to provide comparison data with the AWAC that was deployed at the nearshore development site. Model accuracy was assessed by calculating the bias, root-mean-square-error (RMSE), and Murphy (1988) skill score defined as:

$$skill = 1 - \frac{\sum_{i=1}^N (X_{mod} - X_{obs})^2}{\sum_{i=1}^N (X_{obs} - \bar{X}_{obs})^2} \quad (8)$$

where X_{mod} and X_{obs} are the modelled and observed variables of interest, respectively, and overbars represent time averaging over the length of the time series with N samples. A skill of 1 indicates perfect agreement, 0 indicates the model predictive ability is equivalent to using a mean of the observations, and a skill less than 0 indicates the predictive ability is worse than using a mean of the observations. Here, we consider $0.0 < \text{skill} < 0.5$ to represent “moderate” skill scores, with “high” and “poor” skills for higher and lower scores, respectively [30,31].

Monthly means of the hourly output were used to calculate seasonal and annual wave parameters. Seasons were defined based on the austral summer (December, January, February; DJF), autumn (March, April, May; MAM); winter (June, July, August; JJA); and spring (September, October, November; SON). We also report seasonal anomalies which are calculated relative to the seasonal climatology (e.g. winter anomaly is relative to average of all winters for the 38-year hindcast period) and consider variability as the standard deviation of the variable in question.

As extreme wave events ultimately determine wave energy device survivability (and hence design conditions), we isolated individual storm events from the time series of model-derived wave heights. Storms were identified using a peaks-over-threshold method [32]. The threshold wave height was selected as the largest wave height where the mean residual life plot was approximately linear [32,33]. The storm wave height record was then extracted from the total wave height record by isolating wave peaks that were above the designated wave height threshold (6 m, see below) and separated from previous peaks by at least 24 h, similar to previous analyses of extreme waves along the WA coastline [10,12,13,33]. A Generalized Pareto Distribution (GPD) was then fitted to the storm wave dataset to estimate extreme wave heights associated with annual recurrence intervals (ARI) of interest (e.g. 1, 5, 10, 50, 100 year ARI) [32,33]. Bootstrap confidence intervals for the GPD fit were calculated using 1000 random samples with replacement of the individual storm events described above [34].

2.4. Climate indices

Several climate indices have been identified as potential drivers of wave climate variability along the southern Australian coastline, and more specifically, the south Western Australian coastline. These have included the Southern Annular Mode (SAM) [9,10,25], the position and intensity of the subtropical high-pressure ridge (STRP) [13], and the Southern Oscillation Index (SOI) [9,35]. Below, we provide a brief description of each climate index and how it was used in this analysis.

2.4.1. Southern Annular Mode (SAM)

The SAM, or Antarctic Oscillation, is the zonally symmetric mode of variability in the Southern Hemisphere and arises through an oscillation of air masses between -45 and -60° latitude [36]. The SAM has been linked to storm variability in the Southern Hemisphere that influence both land (e.g. rainfall) and wave climates [2,25,37]. Fluctuations of the SAM from positive to negative phase are associated with the shifting position of the SO storm belt, with positive SAM indicating a southward shift and negative SAM indicating a northward shift of the storm belt. The shifting position of the SO storm belt (and hence SAM phase) has been shown to directly influence both the wave heights and direction of SO-generated swells, with positive SAM driving a decrease in wave heights and counter-clockwise rotation of wave directions along the Australian coastline [9,25]. Daily records of the SAM index were retrieved from NOAA's Climate Prediction Centre (CPC) from 1980 to 2017 (<http://www.cpc.ncep.noaa.gov/products/precip/CWlink/>

[daily_ao_index/ao/ao_index.html](http://www.cpc.ncep.noaa.gov/products/precip/CWlink/daily_ao_index/ao/ao_index.html)). CPC daily SAM values were averaged to monthly values and then seasonal and annual averages were calculated from the monthly means.

2.4.2. Southern Oscillation Index (SOI)

The SOI reflects the fluctuation of the El Niño/Southern Oscillation (ENSO) across the Indo-Pacific region. ENSO is a key predictor of climate in the Pacific as well as wave climates in the Southern Ocean and Australia [10,38]. The SOI is based on the normalised mean sea level pressure difference between Tahiti and Darwin [39,40], with positive values indicating La Niña conditions (increased strength of Pacific trade winds) and negative phases indicating El Niño conditions (decreased strength of Pacific trade winds). Around Western Australia in particular, the SOI has been associated with variability in rainfall, mean sea level, ocean current strength (e.g. Leeuwin Current), and sea level [41–43]. Monthly mean SOI values were retrieved from the Australian Bureau of Meteorology (BOM; <http://www.bom.gov.au/climate/current/soi2.shtml>) and were used to calculate seasonal and annual means.

2.4.3. Subtropical high-pressure ridge position (STRP) and intensity (STRI)

The subtropical high-pressure ridge is a band of anticyclones (high pressure systems) in the mid-latitudes that forms due to descending branch of the Hadley Cell near 30° latitude [44]. The subtropical ridge position (STRP) and intensity (STRI) vary seasonally, with equatorward (north) migration during austral autumn/winter and poleward (south) migration during austral spring/summer [44]. Seasonal variability in STRP and STRI has also been linked to SAM phase [45]. For example, southward shifts in STRP correspond to positive SAM and increased high pressure systems over Western Australia that can block westerly fronts generated in the Southern Ocean [13]. Recently, STRP and STRI have been shown to be key drivers of the wave climate along the western coast of Western Australian (i.e. greater Perth region) [13]. Following Wandres et al. (2018), the STRP and STRI were calculated from the monthly mean sea level pressure (MSLP) fields from the European Centre for Medium Range Forecasts (ECMWF) ERA-Interim data. Monthly STRP and STRI were defined as the latitude and value of the maximum MSLP between 108° to 112° E and -10° to -44° S. Monthly values were then used to calculate seasonal and annual values of both the STRP and STRI.

3. Results

3.1. Model validation

Overlapping time points were extracted from the observational (wave buoy and AWAC) and model records and compared. There exist numerous data gaps of varying lengths (e.g. hours to multiple days) within the DoT buoy record; however, instead of attempting to fill these gaps (e.g. [33]), they were excluded from the analysis as a complete and continuous time series was not needed for model validation. Extracting overlapping time points between the SWAN simulations and the DoT buoy and AWAC observations yielded 102,329 h and 1091 h, respectively, for comparison.

SWAN was able to reproduce the wave conditions measured by the DoT buoy and the AWAC with moderate to high skill for all variables of interest (H_{sig} , T_m , D_m ; Fig. 3). There was a slight over-prediction of H_{sig} at both instrument sites (bias = 0.21 m), and a tendency towards over-predicting small wave heights, but under-predicting large wave heights at the DoT buoy (Fig. 3a). This under-prediction of the largest waves is attributed to the CAWCR hindcast (i.e. the boundary conditions) and is likely related to under-predictions of the upper-most percentile wind speeds

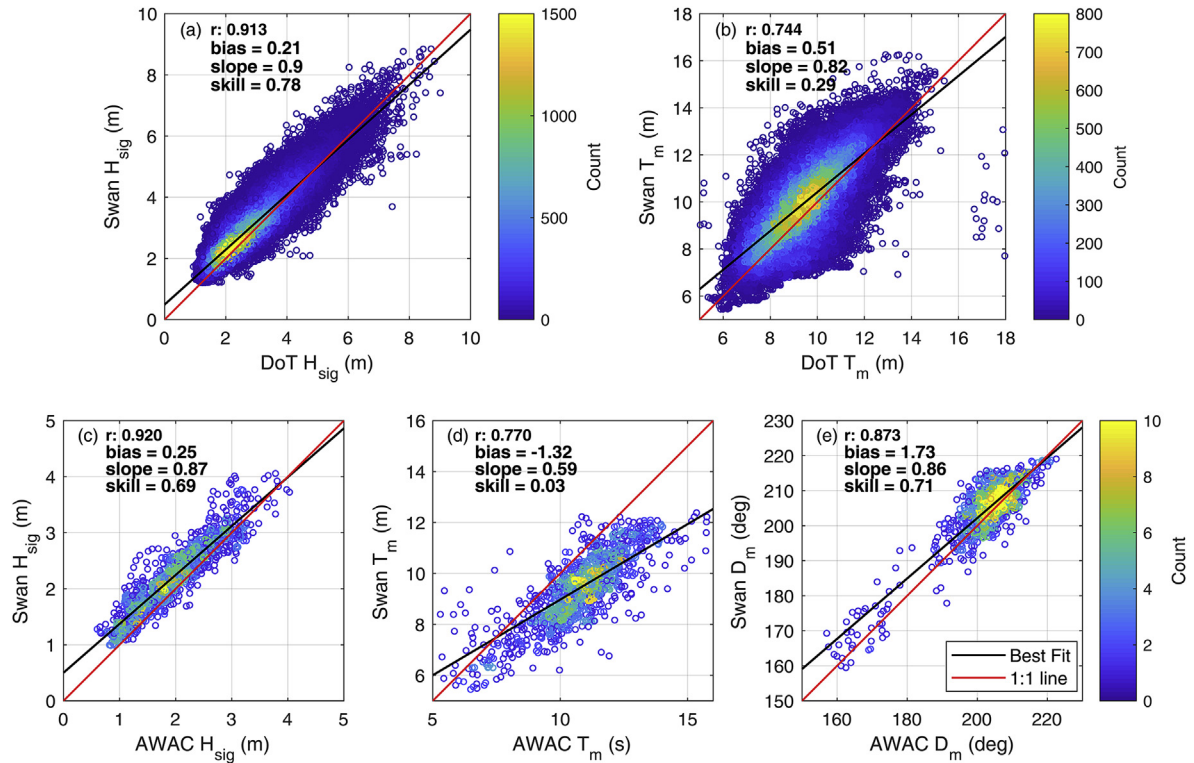


Fig. 3. Model validation at the Department of Transport wave buoy (60 m depth; July 2005 to present) for (a) significant wave height and (b) mean wave period. And comparison at the proposed development site (AWAC in 30 m depth; December 2017 to March 2018) for (c) significant wave height, (d) mean wave period, and (e) mean wave direction.

derived from CFSR winds [21]. T_m was over-predicted at the DoT buoy (bias = 0.51 s) but under-predicted at the AWAC (bias = -1.32 s). T_m at the AWAC tended to be over-predicted for shorter period waves, but under-predicted for the longest period waves (Fig. 3d). The source of these errors is unclear as the bias in T_m could be due to various factors including inaccuracies in SWAN's estimation of the evolution of the wave spectrum across the shelf (i.e. non-linear energy transfers), differences in how T_m was calculated onboard the DoT buoy versus how the AWAC was processed causing the bias to be larger at the AWAC, or there could be some inaccuracies in our derived bathymetry product. There was a small over-prediction of D_m at the AWAC (bias = 2.26°) that was greater when waves were from a more southerly direction (Fig. 3e). There is no directional comparison possible for the DoT buoy

because the two-dimensional spectra data was unavailable from the wave buoy and mean wave direction for the total frequency-directional domain is not calculated by DoT. Although DoT does report peak wave direction (D_p) for 'sea' and 'swell' frequency bins, specific values of D_p depend on the binning of the directional domain, and therefore may mis-represent model accuracy. Finally, given the skill of D_m at the AWAC location and previous validation of wave directions from the CAWCR hindcast [21], no further assessment of wave direction at the DoT buoy was conducted.

3.2. Annual and seasonal wave climate and extreme waves

The wave climate at the development site (calculated from the hourly output for the 38-year simulation) was dominated by waves

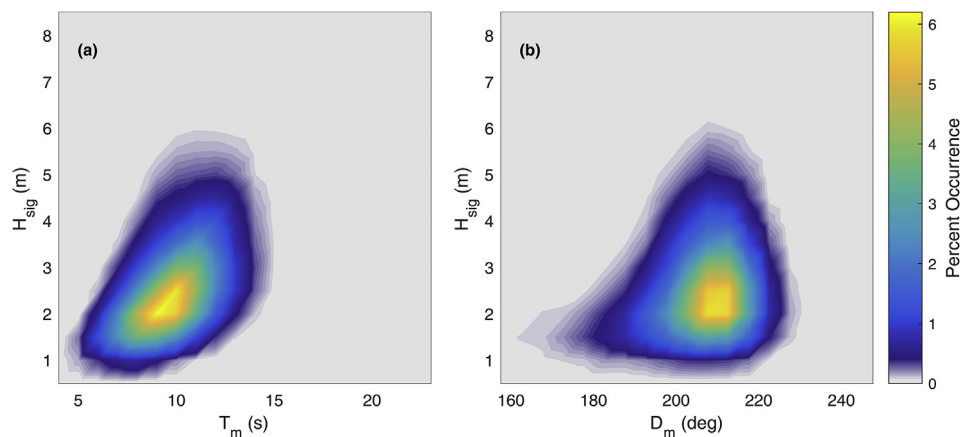


Fig. 4. Joint occurrence distributions for significant wave height and (a) mean period and (b) mean direction at the nearshore development site location (30 m depth) based on the hourly SWAN output from 1980 to 2017.

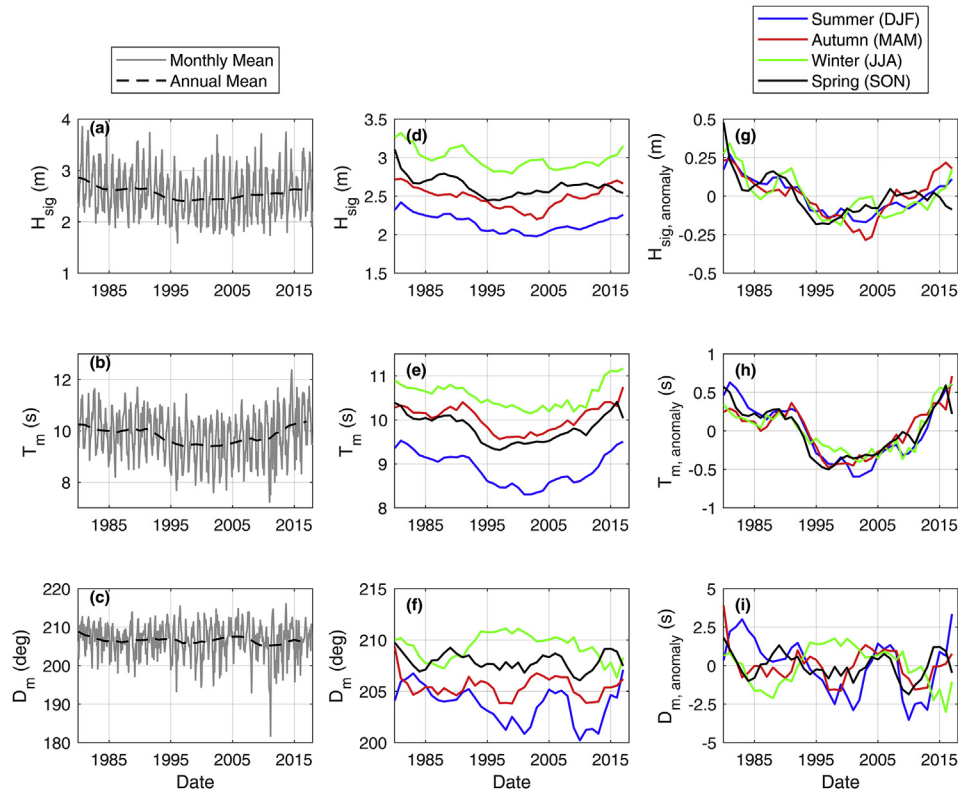


Fig. 5. (a,b,c): Monthly (grey line) and annual (black dashed line, 5-year moving average) means of (a) significant wave height, (b) mean wave period, and (c) mean wave direction at the proposed development site. (d,e,f): Seasonal means (5-year moving average) of (d) significant wave height, (e) mean wave period, and (f) mean wave direction. (g,h,i): Seasonal anomalies (5-year moving average) calculated from the 38-year seasonal climatology for (g) significant wave height, (h) mean wave period, and (i) mean wave direction. For seasonal means, blue represents austral summer (December, January, February), red represents autumn (March, April, May), green represents winter (June, July, August), and black represents spring (September, October, November). (For interpretation of the references to colour in this figure legend, the reader is referred to the Web version of this article.)

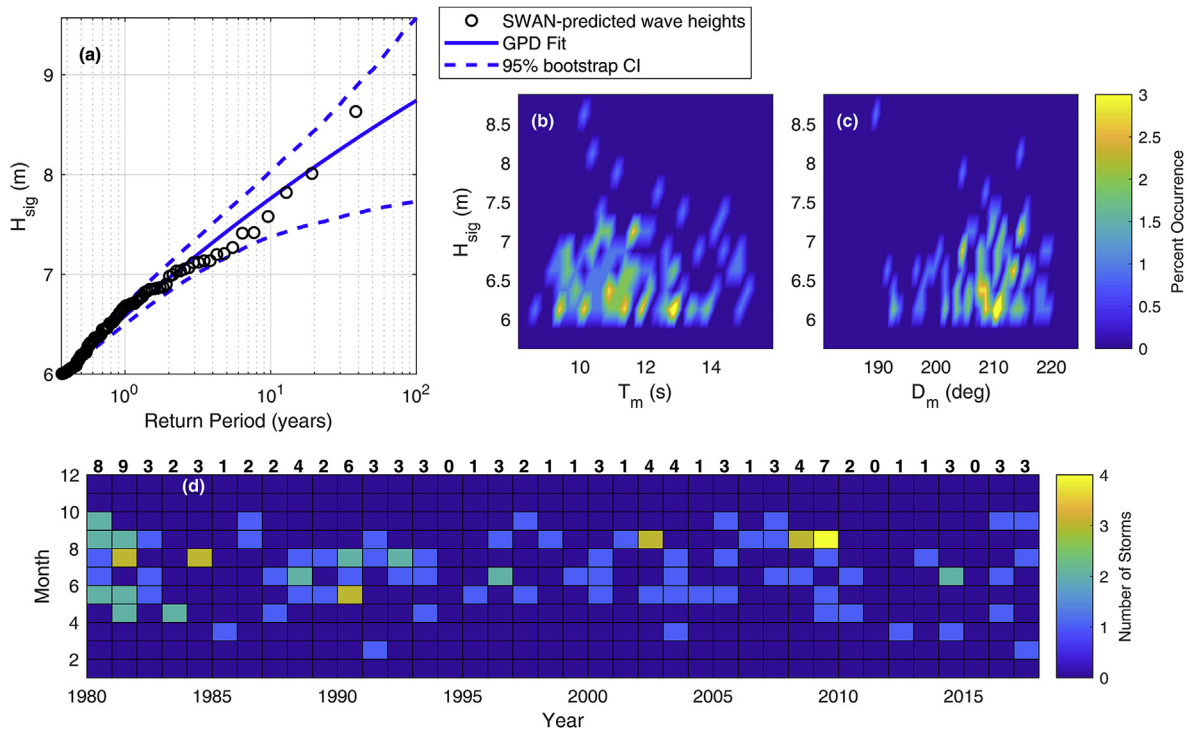


Fig. 6. (a) Extreme value analysis at the shallow water (30 m) development location. Extreme values were calculated using a peaks-over-threshold method, with a threshold of 6 m and de-clustering time interval of 24 h. A Generalized Pareto distribution (GPD) was fit using the maximum product of spacings method with total number of ‘extreme events’ of 104. 95% bootstrap confidence intervals were calculated from 1000 random samples (with replacement) of the extreme event dataset. Joint occurrence distributions of extreme wave heights and (b) mean period and (c) mean direction for all identified storm events. (d) Distribution of storm events ($n = 104$) across the 38-year hindcast (colours indicate number of storms for given month and year); bold numbers on top of panel indicate total number of storm events for corresponding year. (For interpretation of the references to colour in this figure legend, the reader is referred to the Web version of this article.)

with $H_{sig} = 2–3$ m, $T_m = 8–10$ s, and $D_m = 200^\circ–210^\circ$ (Figs. 4 and 5). Seasonally, summer waves were the smallest (mean = 2.15 m) and least variable (standard deviation = 0.14 m), whereas winter waves were the largest (mean = 2.98 m) and most variable (standard deviation = 0.20 m) (Fig. 5b). D_m was more westerly in winter and spring (mean = 209° and 208° , respectively) and more southerly in summer and autumn (mean = 204° and 205° , respectively) (Fig. 5h). Although summer H_{sig} was the least variable of any season, summer D_m was the most variable (standard deviation = 3.2°), with wave events occurring from their most southerly directions (Fig. 5h). T_m also varied seasonally with the smallest values occurring in summer (mean = 8.9 s) and the maximum values in winter (mean = 10.5 s) (Fig. 5e). Fluctuations in seasonal wave height and mean period anomalies (i.e. positive or negative anomalies) occurred during the same year and were of the same magnitude regardless of season (Fig. 5c and f). Mean wave direction anomalies, however, were out of phase between seasons, with winter wave direction anomalies tending to be more southerly (negative anomaly) when summer direction anomalies were positive (more

westerly) (Fig. 5i).

Extreme wave events at the development site were isolated from the wave record using a threshold wave height of 6 m, yielding a total of 104 unique events across the 38-year record (Fig. 6). The 1, 5, 10, 50, and 100 ARI were estimated to be 6.6 m, 7.4 m, 7.8 m, 8.5 m, and 8.7 m, respectively (Fig. 6a). Annually, the total number of storms followed a similar pattern to the annual H_{sig} and H_{sig} anomaly (Fig. 5a and c, respectively), with peaks in total number of large wave events occurring in the early 1990s and again between 2008 and 2010 (Fig. 6d). The total annual number of large wave events varied between 0 and 9 with an average of ~3 storms per year. The stormiest months were July, August, and September, although all months of the year recorded at least one storm event between 1980 and 2017 (Fig. 6d). Large wave events were predominantly from 210° (i.e. similar to modal wave direction); however, there were also several events from a southerly direction (Fig. 6c) which tended to occur during summer months. There was an increasing number of large wave events occurring in August and September later in the record (i.e. after 2005; Fig. 6d).

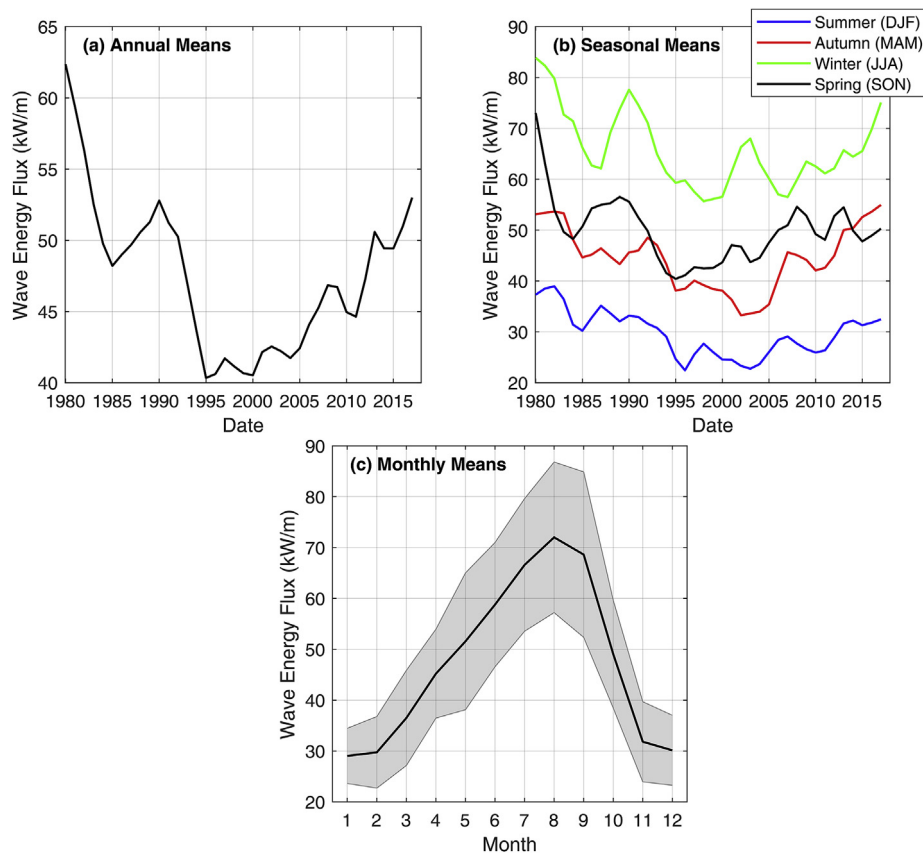


Fig. 7. (a) Annual (5-year moving average), (b) seasonal (5-year moving average), and (c) monthly variability of wave energy flux at the development site. Grey shading in (c) indicates ± 1 standard deviation of the monthly average wave energy flux (solid black line in (c)).

Table 1

Annual and seasonal means and variability of wave energy resource (mean ± 1 standard deviation) for the proposed development site ('shallow water' = 30 m) and a location directly offshore of the nearshore location ('deep water' = 350 m).

	Deep Water Wave Energy Flux (kW/m)	Shallow Water Wave Energy Flux (kW/m)
Annual	65.3 \pm 8.7	47.2 \pm 5.9
Summer (DJF)	37.7 \pm 6.9	29.7 \pm 5.1
Autumn (MAM)	59.3 \pm 10.3	44.4 \pm 7.4
Winter (JJA)	95.1 \pm 14.3	65.3 \pm 9.5
Spring (SON)	69.7 \pm 12.4	49.8 \pm 7.7

3.3. Wave energy resource

The wave energy flux (E_{mag}) incident to Torbay displayed monthly, seasonal, and interannual variability (Fig. 7; Table 1). The annual wave resource at the development site varied between 40

and 60 kW/m (mean 47.2 kW/m; Table 2), with peaks in 1989/1991 and 2015 (Fig. 7a). Winter was consistently the most energetic (and most variable) season across the modelled time period, with the energy flux nearly double that of the summer months (Fig. 7b; Table 2). Monthly average wave power varied from ~30 kW/m in

Table 2
Correlation values (r) for relationships between wave energy flux or mean wave direction and seasonal or annual climate indices in deep (350 m depth) and shallow (30 m depth) water. Bold text indicates significant relationships for the significance threshold $p < 0.1$.

	Deep Water				Shallow Water			
	Emag_anomaly		Dm_anomaly		Emag_anomaly		Dm_anomaly	
	Annual	Seasonal	Annual	Seasonal	Annual	Seasonal	Annual	Seasonal
STRP ^{anomaly}	0.46	0.39	0.65	0.60	0.36	0.28	0.76	0.71
SAM	0.38	0.21	0.29	0.43	0.28	0.09	0.41	0.52
SOI	0.14	0.06	0.45	0.31	0.18	0.07	0.37	0.28

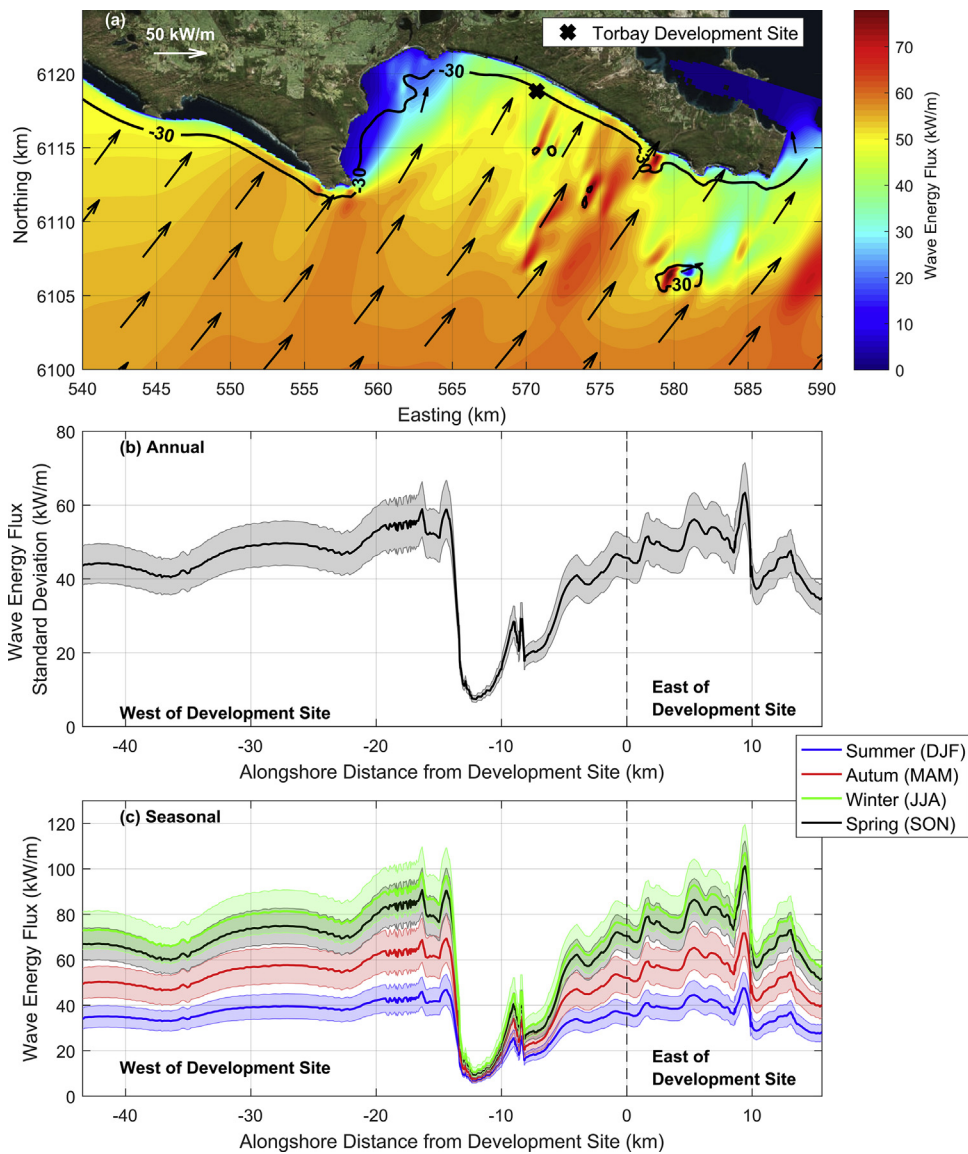


Fig. 8. (a) Spatial distribution for the mean annual wave energy flux and vectors calculated from the monthly spatial distributions for the 38-year hindcast. Proposed development site is marked by black 'x' and 30 m depth contour plotted as black solid line. (b) Mean annual wave energy flux along the 30 m contour (distance is calculated from the proposed development site). Grey shading indicates ± 1 standard deviation. (c) Seasonal mean wave energy flux along the 30 m contour for summer (blue), autumn (red), winter (green), and spring (black). Coloured shading indicates ± 1 standard deviation for the corresponding season. Note, spring and winter shaded regions are overlapping. (For interpretation of the references to colour in this figure legend, the reader is referred to the Web version of this article.)

the summer months to ~ 70 kW/m in the winter months (Fig. 7c).

Annual and seasonal standard deviations of E_{mag} were less than 10 kW/m (Table 1), suggesting a stable and consistent wave energy resource. Spatially, there were areas of consistently higher wave energy within the embayment than the development site (i.e. to the east of the development site; Fig. 8). However, these areas are typically associated with irregular bathymetric features of the bay (including submerged and exposed rock islands; Fig. 1b) that cause localised areas of wave focusing but would also make this area more difficult for subsea wave energy infrastructure. Therefore, when comparing along the whole embayment (Fig. 8), the development site appears to be situated in an ideal position of

consistently high wave power.

3.4. Interannual variability and relationships to climate indices

The time series of wave parameters and energy indicates interannual variability over the 38 years, with the most notable pattern being decreased wave heights, periods, and energy during the late 1990s and early 2000s (Figs. 5 and 7). To assess any coherence between the seasonal variability and the larger-scale synoptic conditions, we compared the seasonal and annual anomalies of E_{mag} and D_m to the seasonal and annual values of the STRP anomaly, SAM, and SOI (Fig. 9). To provide context for changes

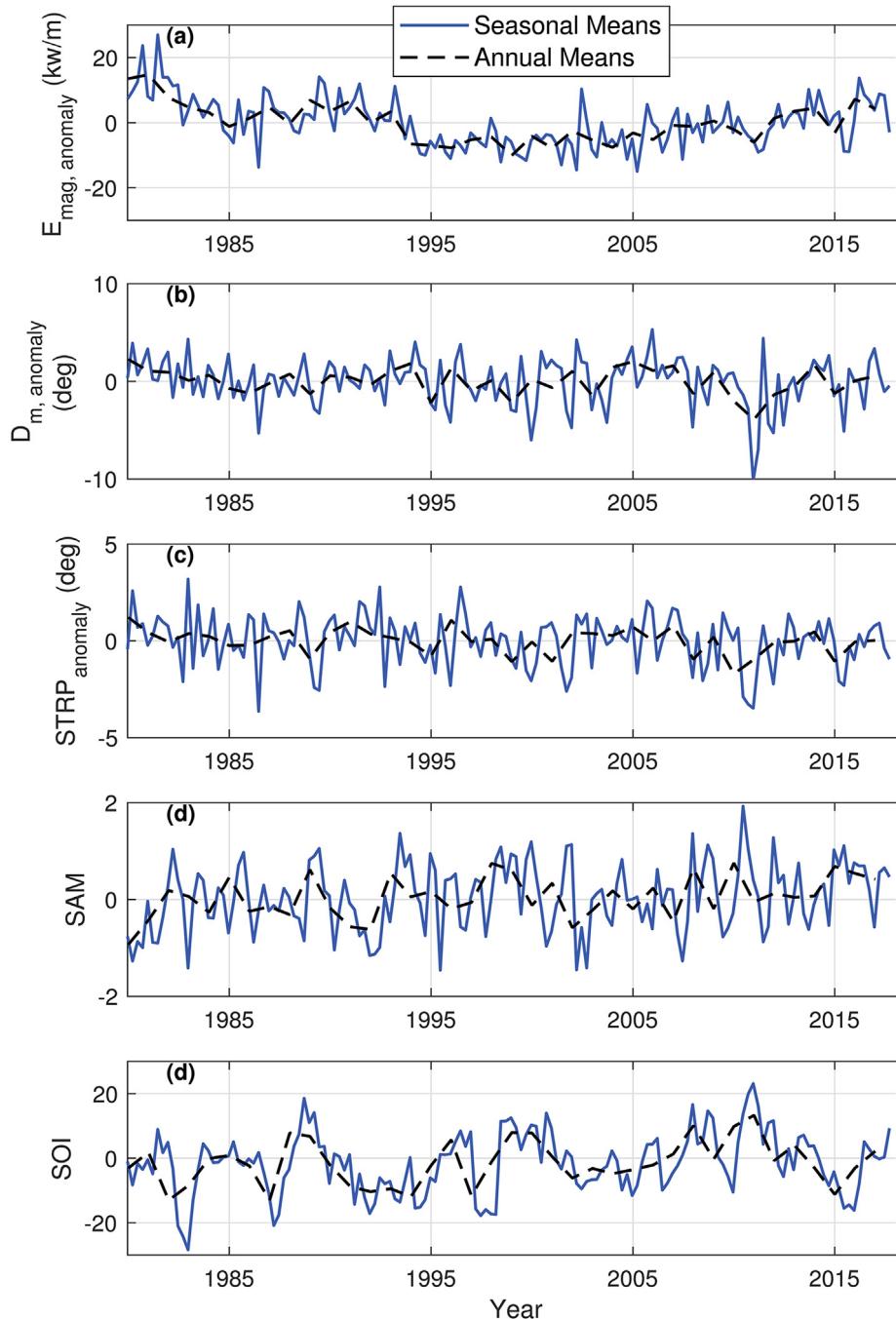


Fig. 9. Seasonal (blue) and annual (black dashed line) means of (a) wave energy flux anomaly and (b) mean wave direction anomaly at the proposed development site and (c) STRP anomaly, (d) SAM phase, and (e) SOI. (For interpretation of the references to colour in this figure legend, the reader is referred to the Web version of this article.)

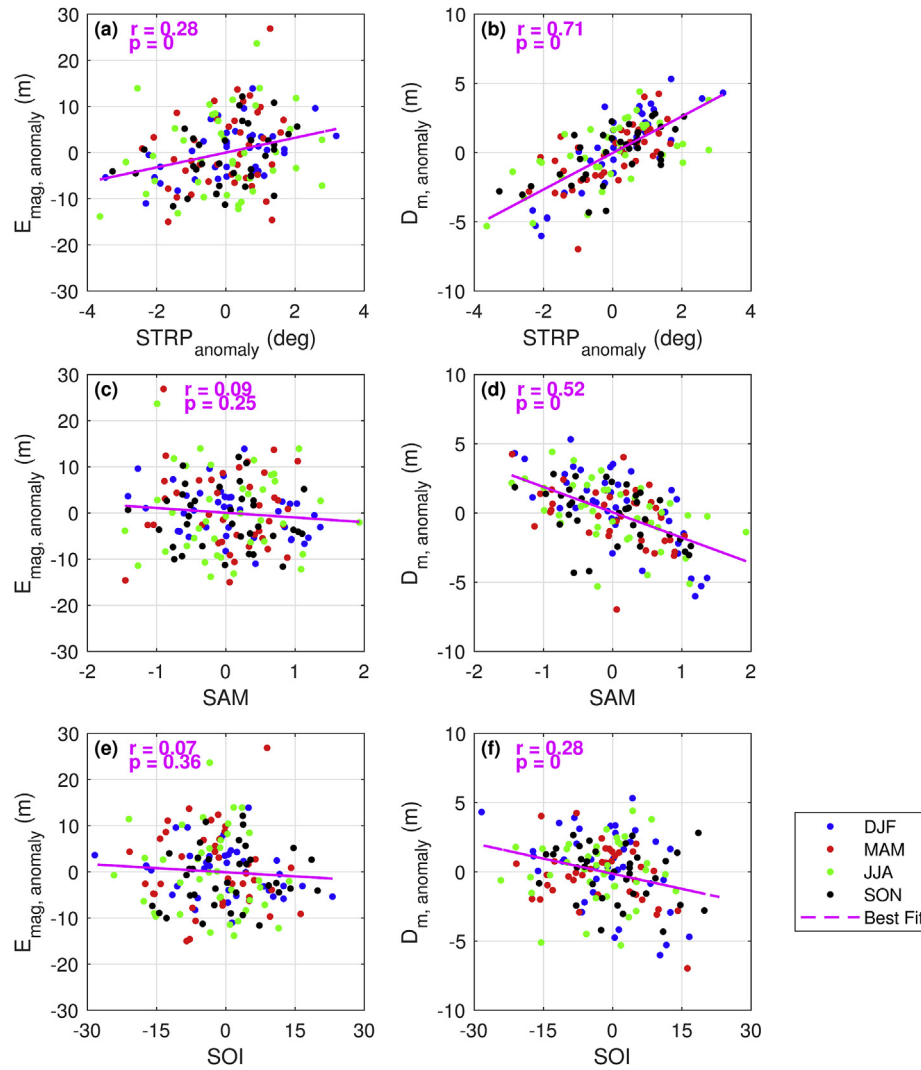


Fig. 10. Relationship between seasonal mean wave energy flux anomaly (first column) or mean wave direction anomaly (second column) and (a,b) STRP anomaly, (c,d) SAM, and (e,f) SOI at the development site (30 m depth). Anomalies were calculated using the 38-year seasonal climatology. Correlation coefficient (r) and p-value (p), which represents the significance of the linear relationship for the significance threshold $p < 0.1$, are included in all panels.

at the development site (30 m depth) and compare with variability of deep water wave climate, this analysis was also conducted at a site directly offshore from the development site in ~350 m depth (Fig. 1).

The wave climate showed a varied response to climate indices across different temporal scales (annual or seasonal) and at different depths (350 m vs. 30 m) (Table 2). In shallow water, STRP had significant relationships to both E_{mag} and D_m at seasonal and annual timescales (Table 2), with positive STRP corresponding to larger E_{mag} (positive anomalies) and more westerly waves (positive anomalies) (Fig. 10a and b and 11a-b). SAM had a significant negative relationship with E_{mag} at annual timescales (positive SAM corresponds to smaller annual E_{mag}) (Fig. 11c; Table 2); however, it showed no relationship with E_{mag} at seasonal timescales (Fig. 10c; Table 2). Although SAM was only related to E_{mag} at annual timescales, SAM had a significant negative relationship with D_m such that positive phases of SAM corresponded to more southerly waves at both annual and seasonal timescales (Figs. 10d and 11d; Table 2). SAM also had a significant negative relationship with the annual number of storm events at the development site (not shown; $r = 0.54$, $p < 0.01$). SOI showed no relationship with E_{mag} at either annual or seasonal timescales (Table 2); however, SOI was

significantly negatively related to D_m at both timescales with positive SOI corresponding to more southerly waves (Fig. 10e and f and 11e-f; Table 2). The deep water site generally exhibited the same relationships as the shallow water site, but the main difference was that the SAM had a significant negative relationship with E_{mag} at seasonal timescales (Table 2).

4. Discussion

4.1. Feasibility of wave energy development at Torbay

Torbay has been targeted by several wave developers and the State of Western Australia as a site for the future development of wave energy converters (WECs). To optimize WEC design and anchoring, as well as to understand the total potential resource, the magnitude and variability of the wave energy resource must be considered. We found that the development site at Torbay has a consistently (i.e. small standard deviation) high wave energy flux on both annual and seasonal timescales (Table 1). When Torbay is compared to other global wave energy development sites [46], it is clear that Torbay presents a unique wave energy resource in that it has one of the largest and most consistent wave energy resources

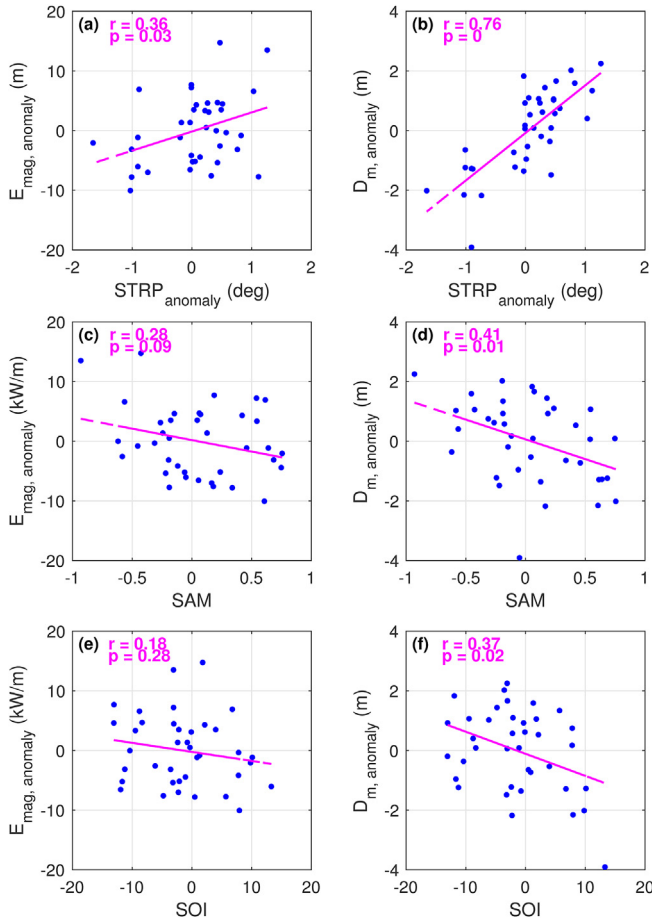


Fig. 11. Relationship between annual mean wave energy flux anomaly (first column) or mean wave direction anomaly (second column) and (a,b) STRP anomaly, (c,d) SAM, and (e,f) SOI at the development site (30 m depth). Anomalies were calculated using the 38-year annual climatology. Correlation coefficient (r) and p -value (p), which represents the significance of the linear relationship for the significance threshold $p < 0.1$, are included in all panels.

(Table 3). Although Gleizon et al. (2017) present wave resources for locations of variable depth (e.g. 155 m–30 m), we normalized the annual average wave energy flux by the seasonal standard deviation to approximate the consistency of the wave energy resource across all locations ('Normalized energy resource'; Table 3). When examining this normalized value, Torbay has the largest potential resource of any reported global location.

Table 3

Comparison of global wave energy hot spots. Global data adapted from Gleizon et al. (2017). Seasonal means are for calculated for respective hemisphere. Normalized energy resource is the annual mean resource normalized by the seasonal variability.

Location	Depth (m)	Annual (kW/m)	Spring (kW/m)	Summer (kW/m)	Autumn (kW/m)	Winter (kW/m)	Seasonal Variability (kW/m)	Normalized Energy Resource
Kerry, IRL	155	64.52	51.7	20.8	68.2	121.6	42.20	1.53
Belmullet, IRL	89	61.88	49.9	20.7	66.9	111.3	37.89	1.63
Nazare, PRT	88	24.1	31	9.5	14.1	42.1	15.11	1.60
Shetlands, GBR	78	40.12	36.2	9.6	37	78.3	28.37	1.41
Sao Vicente, PRT	61	23.1	30.6	8.4	12.6	41.2	15.39	1.50
Orkneys, GBR	54	28.7	27.3	5.9	27.7	54.4	19.86	1.45
Cotentin, FRA	53	5.33	4.2	2.9	5.6	8.1	2.23	2.39
Bretagne, FRA	46	34.12	25.4	12.7	37	64.1	21.91	1.56
Landes, FRA	38	21.89	18.6	7.9	23.4	43.6	14.96	1.46
Hebrides, GBR	30	39.11	39.2	7.9	34.8	75.2	27.66	1.41
Torbay, AUS (this study)*	30	47.2	49.8	29.7	44.4	65.3	14.70	3.21

Table 4

Percentage of time with wave heights between 1 and 4 m (mean \pm standard deviation) at the proposed development site (30 m depth).

	Time (%)
Annual	91.9 \pm 2.3
Summer (DJF)	98.4 \pm 1.2
Autumn (MAM)	94.1 \pm 2.5
Winter (JJA)	84.1 \pm 5.8
Spring (SON)	91.2 \pm 3.7

For this potential resource to be maximized, the conditions must be survivable by WECs and within the energy producing regime specific to each device. Most commercially available (and reported) WECs require wave heights to be above 1 m and less than ~ 4 m to efficiently produce energy [4,24]. Using these criteria, we determined that Torbay wave conditions are within these bounds $\sim 92\%$ of the time (averaged across all annual means) and range from $\sim 84\%$ (winter average) to $\sim 98\%$ (summer average) seasonally (Table 4). However, Torbay regularly experiences large wave events with a 1-year ARI event H_{sig} of 6.6 m and ~ 3 events per year with $H_{sig} > 6$ m (Fig. 6). Therefore, any WECs deployed at Torbay will need to be designed and anchored appropriately to survive several large wave events each year.

To further maximize the available wave energy, it is likely that WECs will be deployed in arrays or 'farms' of varying numbers and spatial density [2,47]. Across the entire alongshore width of Torbay, there are distinct regions of high and low wave energy flux, with annual and seasonal variability equal to or less than that at the development site (Fig. 9). Therefore, there are a range of exploitable wave energy resources that can be utilized by a variety of WECs. For example, the northwest corner of the Torbay embayment (sheltered from dominant SW swells) could be optimized by WECs tailored to exploit ~ 10 – 20 kW/m annually; whereas the development area (± 5 km) could provide a testbed for WECs optimized for 40 – 60 kW/m annually (Fig. 9). Given the alongshore extent of a consistent resource (either 10 – 20 kW/m or 40 – 60 kW/m), WEC farms could consist of 50 – 200 devices depending on array design [47,48]. Torbay therefore provides the unique opportunity for a range of devices to be deployed simultaneously (as WEC farms or individual units) and utilize the same nearshore infrastructure, while also maximizing the range of wave energy regimes typically available globally (i.e. Torbay encompasses the complete range displayed in Table 3).

4.2. Implications for long-term wave energy resource and coastal dynamics

The variability in the nearshore and offshore wave climates at

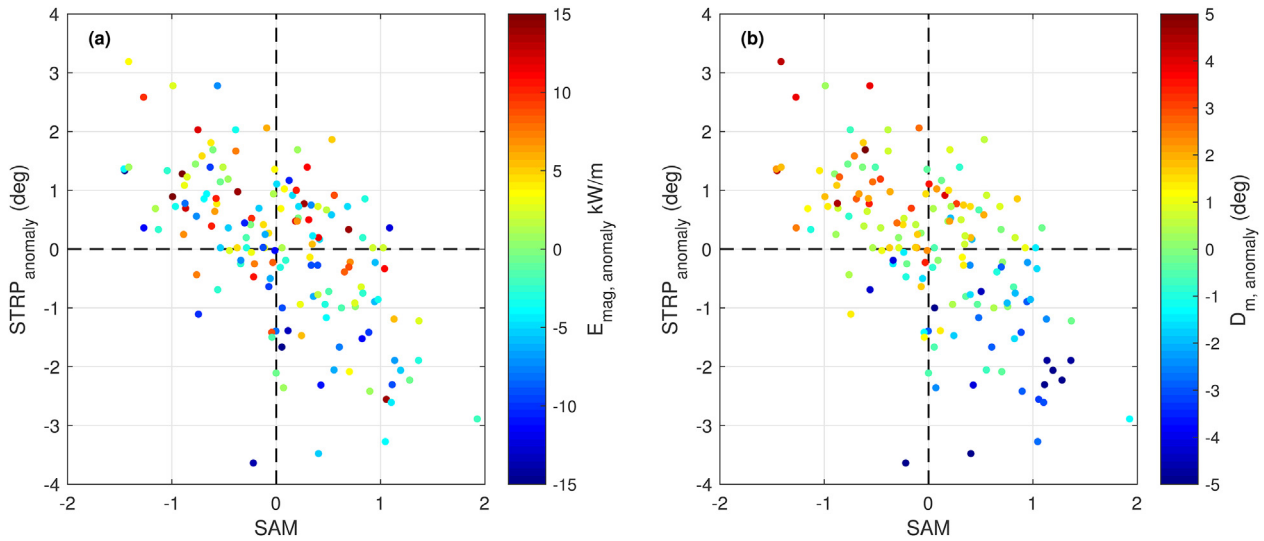


Fig. 12. Relationships between the Southern Annular Mode (SAM), sub-tropical high pressure ridge (STRP), and seasonal mean wave energy flux (a) and seasonal mean wave direction (b) at the development site.

Torbay was shown to be significantly related to the STRP and SAM (Table 2). Similar to recent studies of the Western Australian wave climate [13], our results suggest that STRP is the best indicator of the magnitude and direction of nearshore waves, whereas the SAM is more suited to predicting the offshore wave climate (Table 2; Figs. 10 and 11). However, STRP and SAM are also significantly related to each other at seasonal ($r = 0.36$, $p < 0.05$) and annual ($r = 0.73$, $p < 0.05$) timescales. When considered together, there is a clear trend of positive D_m anomalies during negative SAM phases and northward shifts in STRP (positive STRP anomaly) (Fig. 12b). Similarly, larger E_{mag} generally occurs during negative SAM and positive STRP anomaly (Fig. 12a); however, there are several instances of negative (positive) E_{mag} anomalies during negative (positive) SAM and positive (negative) STRP. For example, winter 1987 had a large positive E_{mag} anomaly (+13 kW/m) and autumn 2001 had a large negative E_{mag} anomaly (−14 kW/m) despite positive SAM and negative STRP in 1987 and negative SAM and positive STRP in 2001. These years had both positive T_m (1987) and negative T_m (2001) anomalies, but neutral H_{sig} anomalies (Fig. 5). Thus, because E_{mag} is dependent on both wave height and period, this variability in E_{mag} is likely related to variability in the Southern Ocean storm belt where more active years correspond to more frequent swell events that can increase average T_m , and subsequently E_{mag} , but may not increase average H_{sig} [10].

Although this study was aimed at understanding wave climate variability in the context of wave energy development, the results have relevance for other applications, including coastal dynamics as the magnitude and direction of wave energy fluxes influence nearshore sediment transport [49]. There is a long-term trend of increasing positive SAM phase [25,36], which, given the relationships observed here (Figs. 10–12; Table 2) is likely to cause poleward shifts in STRP and corresponding decreases in wave energy flux as well as anti-clockwise rotation in wave direction (i.e. shift to more southerly directions). Previous studies have highlighted similar relationships across the Indian Ocean section of the SO and have suggested these trends will likely cause changes to coastal sediment budgets by altering directions of sediment transport [9,13]. However, these studies have lacked the detailed, high-resolution models and bathymetry to investigate these trends in the nearshore zone.

Using our higher-resolution, nearshore model we examined the

relationship between the local alongshore component (E_y , calculated by rotating energy flux vectors from SWAN into local cross-and alongshore directions based on the orientation of the coastline) of the wave energy flux and annual SAM at representative transects along the 10 m depth contour (Fig. 13a). Transects on the western side of the embayment (i.e. T2, T3, T4; Fig. 13a) that are currently sheltered from the predominant wave direction show no relationship between SAM and E_y , whereas transects that are exposed to SW waves, have a significant positive relationship between SAM and E_y (Fig. 13b and c). Thus, as SAM continues to be increasingly positive, our results suggest that the direction of E_y at exposed sections of Torbay (i.e. T1, T5, T6) could change directions and alter sediment transport patterns. Given that most of the southern margin of the Australian continent consists of high energy, wave-dominated embayed beaches similar to Torbay [50], these results suggest that southern Australian beaches may begin to rotate in response to the altered wave directions. Furthermore, should wave farms be developed in the region, the potential changes to the magnitude and direction of the wave energy flux will need to be considered when assessing both the long-term production value and coastal impacts of wave farms [48].

5. Conclusions

The southern Australian coastline has one of the largest wave energy resources reported globally. As wave energy development becomes a greater priority in this region, a higher resolution and more detailed understanding of the nearshore wave climate and wave energy resource at development sites is needed. Here, we used a 38-year wave hindcast to quantify the variability of the nearshore wave climate and local wave energy resource and related these to regional and basin scale climate drivers. The strongest relationships were found between the wave climate and STRP and SAM phase. Both climate indices had effects on the seasonal and annual magnitude and direction of the wave energy flux incident to the study area, with larger and more westerly waves associated with negative phases of SAM and positive (equatorward) STRP. The positive trend in SAM and southward shift in STRP will likely cause anti-clockwise rotation to the wave energy flux vectors, which could have implications for nearshore coastal dynamics (especially if wave farms are developed). Finally, these results suggest that

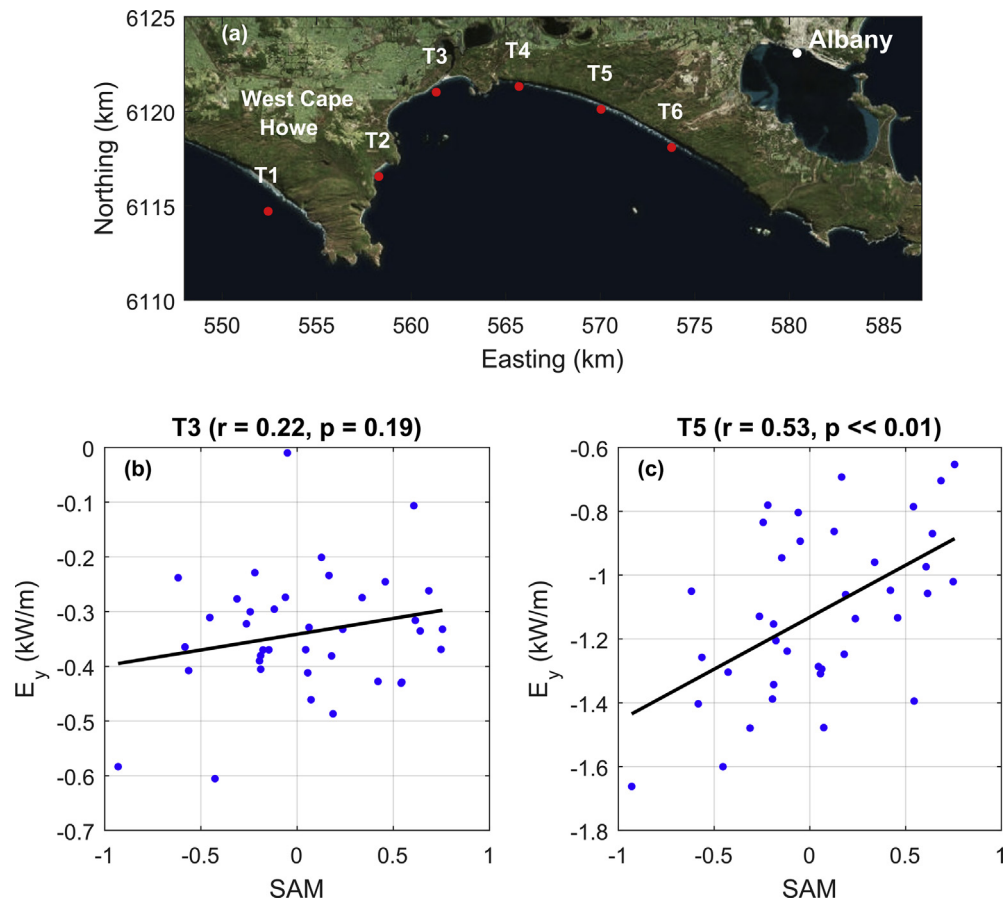


Fig. 13. (a) Overview of Torbay with transects along the 10 m depth contour indicated by red dots. Relationship between local alongshore wave energy flux (E_y) and SAM phase at Transect 3 (b) and Transect 5 (c). Note, sign of E_y indicates direction of flux in local coordinate system; for (b) and (c), negative denotes flux directed towards the East. (For interpretation of the references to colour in this figure legend, the reader is referred to the Web version of this article.)

seasonal and interannual fluctuations in the wave resource can be significant and predictable and therefore, should be considered during the future design of wave energy converters.

Data availability

Data associated with this publication is available online at <https://doi.org/10.5281/zenodo.3253345>, or by request from the corresponding author.

Acknowledgements

This research was conducted by the Wave Energy Research Centre and jointly funded by The University of Western Australia and the Western Australian Government, via the Department of Primary Industries and Regional Development (DPIRD). We also acknowledge funding from the Australian Renewable Energy Agency (ARENA) as part of ARENA's Research and Development Programme (grant number 2015RND086). This work was supported by resources provided by the Pawsey Supercomputing Centre with funding from the Australian Government and the Government of Western Australia. We thank two anonymous reviewers for constructive comments that helped to improve this manuscript.

References

- [1] I.R. Young, Seasonal variability of the global ocean wind and wave climate, *Int. J. Climatol.* 19 (1999) 931–950, [https://doi.org/10.1002/\(SICI\)1097-0088\(199907\)19:9<931::AID-JOC412>3.0.CO;2-O](https://doi.org/10.1002/(SICI)1097-0088(199907)19:9<931::AID-JOC412>3.0.CO;2-O).
- [2] B.G. Reguero, I.J. Losada, F.J. Méndez, A global wave power resource and its seasonal, interannual and long-term variability, *Appl. Energy* 148 (2015) 366–380, <https://doi.org/10.1016/j.apenergy.2015.03.114>.
- [3] K. Gunn, C. Stock-Williams, Quantifying the global wave power resource, *Renew. Energy* 44 (2012) 296–304, <https://doi.org/10.1016/j.renene.2012.01.101>.
- [4] M.A. Hemer, S. Zieger, T. Durrant, J.O. Grady, R.K. Hoeke, K.L. McInnes, U. Rosebrock, A revised assessment of Australia's national wave energy resource, *Renew. Energy* 114 (2016) 1–23, <https://doi.org/10.1016/j.renene.2016.08.039>.
- [5] IEC, International Electrotechnical Commission Technical Committee, *Marine Energy e Wave, tidal and other water current converters e Part 101: Wave energy resource assessment and characterization*, 2015.
- [6] T. Durrant, M. Hemer, G. Smith, C. Trenham, D. Greensade, CAWCR Wave Hindcase Extension June 2013 - July 2014, 2015. <http://doi.org/10.4225/08/55C99193B3A63>.
- [7] M.A. Hemer, D.A. Griffin, The wave energy resource along Australia's Southern margin, *J. Renew. Sustain. Energy* 2 (2010) 1–15, <https://doi.org/10.1063/1.3464753>.
- [8] M.G. Hughes, A.D. Heap, National-scale wave energy resource assessment for Australia, *Renew. Energy* 35 (2010) 1783–1791, <https://doi.org/10.1016/j.renene.2009.11.001>.
- [9] M.A. Hemer, J.A. Church, J.R. Hunter, Variability and trends in the directional wave climate of the Southern Hemisphere, *Int. J. Climatol.* 30 (2010) 475–491, <https://doi.org/10.1002/joc.1900>.
- [10] C. Bosserelle, C. Pattiaratchi, I. Haigh, Inter-annual variability and longer-term changes in the wave climate of Western Australia between 1970 and 2009, *Ocean Dyn.* 62 (2012) 63–76, <https://doi.org/10.1007/s10236-011-0487-3>.
- [11] M.A. Hemer, D.A. Griffin, The wave energy resource along Australia's Southern margin, *J. Renew. Sustain. Energy* 2 (2010), <https://doi.org/10.1063/1.3464753>.
- [12] A.J. Lemm, B.J. Hegge, G. Masselink, Offshore wave climate, Perth (western Australia), 1994–1996, *Mar. Freshw. Res.* 50 (1999) 95–102, <https://doi.org/10.1071/mf99092>.

[1] I.R. Young, Seasonal variability of the global ocean wind and wave climate, *Int.*

- [13] M. Wandres, C. Pattiaratchi, Y. Hetzel, E.M.S. Wijeratne, The response of the southwest Western Australian wave climate to Indian Ocean climate variability, *Clim. Dyn.* 50 (2018) 1533–1557, <https://doi.org/10.1007/s00382-017-3704-z>.
- [14] G. Masselink, C.B. Pattiaratchi, Seasonal changes in beach morphology along the sheltered coastline of Perth, Western Australia, *Mar. Geol.* 172 (2001) 243–263, [https://doi.org/10.1016/S0025-3227\(00\)00128-6](https://doi.org/10.1016/S0025-3227(00)00128-6).
- [15] A.A.J. Williams, R.C. Stone, An assessment of relationships between the Australian subtropical ridge, rainfall variability, and high-latitude circulation patterns, *Int. J. Climatol.* 28 (2009) 691–709, <https://doi.org/10.1002/joc>.
- [16] L.E.E. Segura, J.E.E. Hansen, R.J.J. Lowe, G. Symonds, S. Contardo, Shoreline variability at a low-energy beach: contributions of storms, megacusps and sea-breeze cycles, *Mar. Geol.* 400 (2018) 94–106, <https://doi.org/10.1016/j.margeo.2018.03.008>.
- [17] N. Booij, R.C. Ris, L.H. Holthuijsen, A third-generation wave model for coastal regions: 1. Model description and validation, *J. Geophys. Res. Ocean.* 104 (1999) 7649–7666, <https://doi.org/10.1029/98JC02622>.
- [18] R.C. Ris, L.H. Holthuijsen, N. Booij, A third-generation wave model for coastal regions: Verification, *J. Geophys. Res.* 104 (1999) 7667, <https://doi.org/10.1029/1998JC900123>.
- [19] G. Australia, 50m Multibeam Dataset of Australia, 2012. <https://ecat.ga.gov.au/geonetwork/srv/eng/catalog.search?node=srv#/metadata/bc422803-0ab4-5350-e044-0014fdd4fa6>.
- [20] H.L. Tolman, User manual and system documentation of WAVEWATCH-IIITM version 3.14, Tech. Note (2009) 220, <https://doi.org/10.3390/ijerph2006030011>.
- [21] T. Durrant, D. Greenslade, M. Hemar, C. Trenham, CAWCR Technical Report No. 070: A Global Hindcast Focussed on the Central and South Pacific, 2014.
- [22] S. Saha, S. Moorthi, H.L. Pan, X. Wu, J.J. Wang, S. Nadiga, P. Tripp, R. Kistler, J. Woollen, D. Behringer, H. Liu, D. Stokes, R. Grumbine, G. Gayno, J.J. Wang, Y.T. Hou, H.Y. Chuang, H.M.H. Juang, J. Sela, M. Iredell, R. Treadon, D. Kleist, P. Van Delst, D. Keyser, J. Derber, M. Ek, J. Meng, H. Wei, R. Yang, S. Lord, H. Van Den Dool, A. Kumar, W. Wang, C. Long, M. Chelliah, Y. Xue, B. Huang, J.K. Schemm, W. Ebisuzaki, R. Lin, P. Xie, M. Chen, S. Zhou, W. Higgins, C.Z. Zou, Q. Liu, Y. Chen, Y. Han, L. Cucurull, R.W. Reynolds, G. Rutledge, M. Goldberg, The NCEP climate forecast system reanalysis, *Bull. Am. Meteorol. Soc.* 91 (2010) 1015–1057, <https://doi.org/10.1175/2010BAMS3001.1>.
- [23] A. Chawla, D. Spindler, H.L. Tolman, A thirty year wave hindcast using the latest NCEP climate forecast system reanalysis winds, *Int. Work. Wave Hindcasting Forecast 70* (2011) 1–11.
- [24] J. Morim, N. Cartwright, A. Etamad-Shahidi, D. Strauss, M. Hemer, Wave energy resource assessment along the Southeast coast of Australia on the basis of a 31-year hindcast, *Appl. Energy* 184 (2016) 276–297, <https://doi.org/10.1016/j.apenergy.2016.09.064>.
- [25] A.G. Marshall, M.A. Hemer, H.H. Hendon, K.L. McInnes, A.G. Marshall, M.A. Hemer, Southern Annular Mode impacts on global ocean surface waves, *Ocean Model.* 129 (2018) 58–74, <https://doi.org/10.1016/j.ocemod.2018.07.007>.
- [26] K. Hasselmann, T.P. Barnett, E. Bouws, H. Carlson, D.E. Carwright, K. Enke, J.A. Ewing, H. Gienapp, D.E. Hasselmann, P. Kruseman, A. Meerburg, P. Muller, D.J. Olbers, K. Richter, W. Sell, H. Walden, Measurements of Wind-Wave Growth and Swell Decay during the Joint North Sea Wave Project, JONS-WAP, 1973.
- [27] A.J. van der Westhuysen, M. Zijlema, J.A. Battjes, Nonlinear saturation-based whitecapping dissipation in SWAN for deep and shallow water, *Coast. Eng.* 54 (2007) 151–170, <https://doi.org/10.1016/j.coastaleng.2006.08.006>.
- [28] S. Hasselmann, K. Hasselmann, J.H. Allender, T.P. Barnett, Computations and parameterizations of the nonlinear energy transfer in a gravity-wave spectrum. Part II: parameterizations of the nonlinear energy transfer for application in wave models, *J. Phys. Oceanogr.* 15 (1985) 1378–1391.
- [29] Y. Eldeberky, Nonlinear Transformation of Wave Spectra in the Nearshore Zone, Delft University of Technology, 1996.
- [30] J.E. Hansen, B. Raubenheimer, J.H. List, S. Elgar, Modeled alongshore circulation and force balances onshore of a submarine canyon, *J. Geophys. Res. Ocean.* 120 (2015) 1887–1903, <https://doi.org/10.1002/2014JC010320>. Received.
- [31] M.V.W. Cuttler, J.E. Hansen, R.J. Lowe, E.J.F. Drost, Response of a fringing reef coastline to the direct impact of a tropical cyclone, *Limnol. Oceanogr. Lett.* 3 (2018) 31–38, <https://doi.org/10.1002/lol2.10067>.
- [32] S. Coles, J. Bawa, L. Trenner, P. Dorazio, *An Introduction to Statistical Modeling of Extreme Values*, 2001.
- [33] F. Li, C. Bicknell, R. Lowry, Y. Li, A comparison of extreme wave analysis methods with 1994–2010 offshore Perth dataset, *Coast. Eng.* 69 (2012) 1–11, <https://doi.org/10.1016/j.coastaleng.2012.05.006>.
- [34] B. Efron, R. Tibshirani, [Bootstrap methods for standard errors, confidence intervals, and other measures of statistical accuracy]: rejoinder, *Stat. Sci.* 1 (1986) 54–75, <https://doi.org/10.1214/ss/1177013817>.
- [35] M.A. Hemer, Historical trends in Southern Ocean storminess: long-term variability of extreme wave heights at cape Sorell, Tasmania, *Geophys. Res. Lett.* 37 (2010), <https://doi.org/10.1029/2010GL044595> n/a–n/a.
- [36] G.J. Marshall, Trends in the Southern annular mode from observations and reanalyses, *J. Clim.* 16 (2003) 4134–4143, [https://doi.org/10.1175/1520-0442\(2003\)016<4134:TTSAM>2.0.CO;2](https://doi.org/10.1175/1520-0442(2003)016<4134:TTSAM>2.0.CO;2).
- [37] A.G. Marshall, D. Hudson, M.C. Wheeler, H.H. Hendon, O. Alves, Simulation and prediction of the Southern Annular Mode and its influence on Australian intra-seasonal climate in POAMA, *Clim. Dyn.* 38 (2012) 2483–2502, <https://doi.org/10.1007/s00382-011-1140-z>.
- [38] T.R. Mortlock, I.D. Goodwin, Directional wave climate and power variability along the Southeast Australian shelf, *Cont. Shelf Res.* 98 (2015) 36–53, <https://doi.org/10.1016/j.csr.2015.02.007>.
- [39] C.F. Ropelewski, P.D. Jones, An extension of the Tahiti-Darwin southern oscillation index, *Mon. Weather Rev.* 115 (1987) 2161–2165.
- [40] W.Y. Chen, Fluctuations in northern Hemisphere 700 mb height field association with the southern oscillation, *Mon. Weather Rev.* 110 (1982) 808–823.
- [41] M. Feng, G. Meyers, A. Pearce, S. Wijffels, Annual and interannual variations of the leewind current at 32°S, *J. Geophys. Res.* 108 (2003) 3355, <https://doi.org/10.1029/2002JC001763>.
- [42] N. Telcic, C. Pattiaratchi, Influence of northwest cloudbands on southwest Australian rainfall, *J. Climatol.* (2014) 11, <https://doi.org/10.1155/2014/671394>.
- [43] F.H.S. Chiew, T.C. Piechota, J.A. Dracup, T.A. McMahon, El Nino/Southern Oscillation and Australian rainfall, streamflow and drought: links and potential for forecasting, *J. Hydrol.* 204 (1998) 138–149, [https://doi.org/10.1016/S0022-1694\(97\)00121-2](https://doi.org/10.1016/S0022-1694(97)00121-2).
- [44] W. Cai, P. van Rensch, T. Cowan, Influence of global-scale variability on the subtropical ridge over Southeast Australia, *J. Clim.* 24 (2011) 6035–6053, <https://doi.org/10.1175/2011JCLI4149.1>.
- [45] A. Williams, R. Stone, An assessment of relationships between the Australian subtropical ridge, rainfall variability, and high-latitude circulation patterns, *International J. Climatol.* 29 (2009) 691–709, <https://doi.org/10.1002/joc>.
- [46] P. Gleizon, F. Campuzano, P. Carracedo, A. Martinez, J. Goggins, R. Atan, S. Nash, Wave Energy Resources along the European Atlantic Coast, Springer International Publishing, 2017, https://doi.org/10.1007/978-3-319-53536-4_2.
- [47] S. Behrens, J.A. Hayward, S.C. Woodman, M.A. Hemer, M. Ayre, Wave energy for Australia's national electricity market, *Renew. Energy.* 81 (2015) 685–693, <https://doi.org/10.1016/j.renene.2015.03.076>.
- [48] D.P. Rijnsdorp, J. Hansen, R. Lowe, Improving predictions of the coastal impacts of wave farms using a phase-resolving wave model, *Coast. Eng.* (2017) 1–5.
- [49] P.D. Komar, D.L. Inman, Longshore Sand Transport on Beaches in and near and compute and spectra [Koontz and p are . respectively the sand and tools began in 1966, in: A Preliminary Report for Pore Space and Can Be Taken it Is Inman Verified that the Longshore Advantageous to Ex, vol. 75, 1970, pp. 5914–5927.
- [50] A.D. Short, Australian beach systems—nature and distribution, *J. Coast. Res.* 221 (2006) 11–27, <https://doi.org/10.2112/05A-0002.1>.